FRONTIERS OF PHYSICS

RESEARCH ARTICLE
Volume 18 / Issue 4 / 42301 / 2023

An ultra-wideband coding polarizer for beam control and RCS reduction

Huanhuan Gao[1], Xiaojun Huang[1,†], Xiongwei Ma[1], Xiaoyan Li[2], Linyan Guo[3], Helin Yang[4,‡]

1 College of Communication and Information Engineering, Xi'an University of Science and Technology, Xi'an 710054, China
2 College of Physical Science and Technology, Northwestern Polytechnical University, Xi'an 710129, China
3 School of Geophysics and Information Technology, China University of Geosciences, Beijing 100083, China
4 College of Physical Science and Technology, Central China Normal University, Wuhan 430079, China
Corresponding authors. E-mail: †hxj@xust.edu.cn, ‡emyang@mail.ccnu.edu.cn
Received September 24, 2022; accepted December 27, 2022

ABSTRACT

Pancharatnam–Berry (PB) phase metasurface, as a special class of gradient metasurfaces, has been paid much attention owing to the robust performance for phase control of circularly polarized waves. Herein, we present an element-based polarizer for the first step, which enables the incident electromagnetic waves into the cross-polarized waves with the relative bandwidth of 71%, and the polarization conversion ratio exceeds 90% at 6.9–14.5 GHz. Then an eight-elements coding polarizer based on the PB phase is presented for the applications on beam control and radar cross section reduction. The simulated values indicate that the reduction of radar cross section is more than 10 dB at 6–16 GHz. Our work reveals the availability of manipulating the waves, beamforming in communication systems and electromagnetic stealth, and so on.

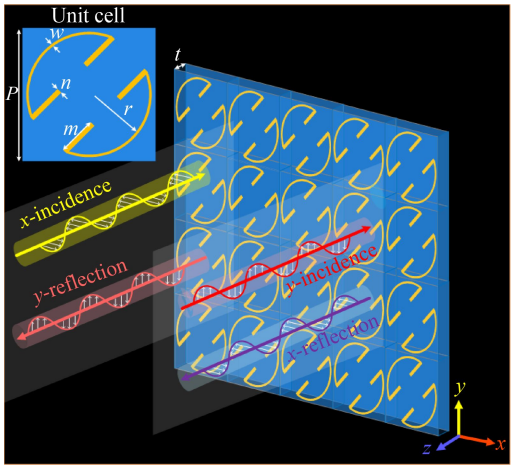

Keywords polarizer, Pancharatnam–Berry phase, coding metasurface, beam control, RCS reduction

1 Introduction

Metasurface (MS) has attracted great interest in terms of arbitrarily controlling electromagnetic (EM) waves, which is flexibly arranged to alter the phase, amplitude, polarization state and other different characteristics [1–5]. Many different structured MSs have been designed to achieve polarization conversion [6–13]. Conventional MS controls the propagation of EM waves by accumulating progressively changing phases, which requires careful design of the spatial distribution of MS geometry. Recently, a new approach to shape light beams by introducing abrupt phase has been proposed to develop many applications for flexible manipulation of EM waves [14], such as vortex beam [15], abnormal reflection and refraction [16, 17], beam separation [18], beam diffusion [19], and beam focusing [20, 21].

An effective way to achieve the desired abrupt phase is varying the geometric dimension of cell structure, which has been reported in a large number of references [22–25]. Pancharatnam–Berry (PB) phase elements can be introduced by adjusting orientation [26]. The control of PB phase by rotation of each meta-atom at a certain angle is the most popular way due to its convenience and robustness. There are abundant different applications have been introduced, as for wave control in the free space, such as meta-lens [27, 28], holograms [29], airy beam generation [30], orbital angular momentum [31], cloaking [32, 33] and other applications [34].

PB MS has a strong ability to control EM waves in

https://doi.org/10.1007/s11467-022-1252-4

terahertz and visible range [19, 31, 35, 36]. Recently, beam control is extended to microwave band, which can improve the channel capacity but suffer from narrow band and low efficiency [37, 38]. For example, anomalous reflection and diffusion was realized for two circular polarizations independently in the 12–18 GHz frequency range [39]. To break the limits of inefficiency and narrow bandwidth, two PB unit cells were presented and manufactured for realizing spin hall effect and focusing effect within 8.2–17.3 GHz [40]. A PB coding metasurface (CMS) was proposed to manipulate broadband arbitrary reflective wave in the range of 16–24 GHz [41]. A CMS with polarization insensitivity was presented to manipulate the scattering of EM waves in dual-broadband of 9.26–12.87 GHz and 14.84–19.35 GHz [42]. In addition, one of the most significant applications of beam control is EM stealth [43], which reduces the radar cross section (RCS) of targets by designing MS structures in a scattering-like [44–47], rather than the reshaping [48] or absorber [49]. Thus, it is desirable to improve the bandwidth and efficiency of beam control in the microwave field.

In this paper, we present a new basic MS unit arranged in a coding manner to apply in circularly polarized beam control and RCS reduction to improve the bandwidth and performance. The basic unit converts the incident waves into a reflected cross-polarized waves, and its PCR ranges from 6.9 GHz to 14.5 GHz above 90%. Moreover, CMSs based on the PB phase principle are arranged to manipulate circularly beam, which can achieve abnormal reflection, beam separation and other phenomena. We randomly arrange the CMS and verify that it plays a role in RCS reduction for a wideband frequency range. This work has a potential application in EM stealth and antenna design.

2 Theoretical analysis of far-field scattering

Based on the reflection theory, cross polarization does not exist in u- and v-polarization incidence due to the symmetry of anisotropic unit cell [48]. When u- and v-axis overlap with x–y axis, $r_{xx} = r_{uu}$, $r_{yy} = r_{vv}$. The reflection matrix can be described as

$$R_{lin}=\begin{pmatrix}\cos\varphi & -\sin\varphi\\ \sin\varphi & \cos\varphi\end{pmatrix}^{-1}\begin{pmatrix}r_{uu} & 0\\ 0 & r_{vv}\end{pmatrix}\begin{pmatrix}\cos\varphi & -\sin\varphi\\ \sin\varphi & \cos\varphi\end{pmatrix}. \tag{1}$$

At this point, the circularly polarized incident reflection matrix is

$$R_{cir}=\frac{1}{2}\begin{pmatrix}1 & -j\\ 1 & j\end{pmatrix}R_{lin}\begin{pmatrix}1 & -j\\ 1 & j\end{pmatrix}^{-1}=\begin{pmatrix}r_{-+} & r_{--}\\ r_{++} & r_{+-}\end{pmatrix}, \tag{2}$$

where φ represents the angle of rotation between the positive u-axis and x-axis. R_{lin} and R_{cir} denote the reflection coefficient matrix of linearly polarized wave and circularly polarized wave, respectively. The right- and left-handed states of circularly polarized waves are denoted by subscripts + and –, respectively. Gradient metasurface can be designed in conjunction with the PB phase theory and plays a part in the anomalous reflection of circularly polarized waves. First of all, the reflection amplitude of the circularly polarized waves remains unchanged and realizes reflection phase shift of $\pm 2\varphi$, therefore, the phase gradient would be produced:

$$\nabla\alpha=\frac{\pm 2\varphi}{P}=\frac{\pm 2\pi}{L}, \tag{3}$$

where $L = NP$, N represents the amount of subunit structures. When the incident wave is vertically incident ($\theta_i = 0$), the anomalous reflection angle is expressed as [16]

$$\theta_r=\frac{k_0\sin\theta_i+\nabla\alpha}{k_0}, \tag{4}$$

where $k_0 = 2\pi/\lambda$ and θ_i imply the wave vector in free space and the angle of incident angle, respectively. Equation (4) can be simplified as $\theta_r = \arcsin(\pm\lambda/L)$.

Then a CMS consists of $N\times N$ array elements, each of which consists of $M\times M$ array of basic units. The schematic diagram of the scattered field of metasurface, as shown in Fig. 1. Due to the destructive elimination of CMS, the plane wave is positively incident, the far-field function can be indicated as

$$F(\theta,\varphi)=\sum_{m=1}^{M}\exp\{-\mathrm{i}k_0D_x\left(m-\frac{1}{2}\right)\sin\theta\cos\varphi+m\pi\}\cdot\sum_{n=1}^{N}\exp\{-\mathrm{i}k_0D_y\left(n-\frac{1}{2}\right)\sin\theta\cos\varphi+n\pi\}. \tag{5}$$

D_x and D_y represent the length of basic elements. When

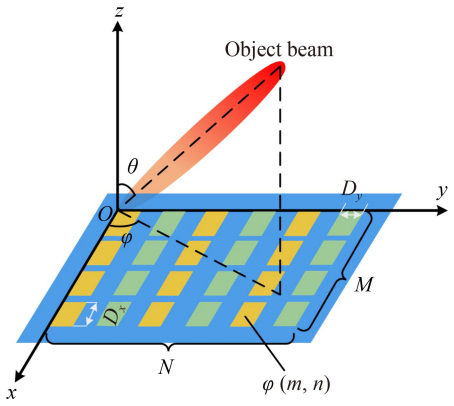

Fig. 1 Structure diagram.

the designed CMS is arranged along x- or y-axis, θ and φ can be described as

$$\begin{cases} \varphi = \pi \pm \arctan\dfrac{D_x}{D_y}, \\ \theta = \arcsin\left(\dfrac{\lambda}{2}\right)\sqrt{\dfrac{1}{D_y^2}+\dfrac{1}{D_x^2}}. \end{cases} \tag{6}$$

3 Design and simulation

To design a polarization converter with excellent performance, it is necessary to achieve as high a cross-polarization reflectance and as low co-polarization reflectance as possible over the ultra-wide frequency band. This will lead to a high polarization conversion rate (PCR) and a perfect polarization conversion. Therefore, based on the theory of eigen-mode analysis [50], it is known that the polarizer stucture needs to symmetrical along the u-axis. Figure 2 shows an ultra-broadband polarizer, which is consisted of two copper layers sandwiched by a dielectric substrate. The structure enables the incident waves to undergo complete reflection without transmission because of the bottom copper plate. FR4 is used as the dielectric slab and its dielectric constant and tangent loss are 4.3 and 0.025, respectively. The metal layer adopts a copper film with an electrical conductivity of 5.8×10^7 S/m and a thickness of 0.035 mm. The optimized dimension of the polarizer of the structure are $t = 3$ mm, P = 5.1 mm, $r = 2.3$ mm, $w = 0.1$ mm, $m = 1.5$ mm, $n =$ 0.2 mm.

The response of the forward incident EM wave can be simulated using CST Microwave Studio. The simulated reflectance of r_{xx} and r_{yx} in 4–18 GHz are depicted in Fig. 3(a). The reflection coefficient r_{yx} reaches more than –1 dB in 6.9–14.5 GHz representing the polarization conversion that occurs. Simultaneously, the co-polarized reflectance r_{xx} is lower than –10 dB. Thus, we can draw a conclusion that the x-polarized wave is mainly reflected and converts into y-polarized wave. Conspicuously, the reflectances of r_{yx} and r_{xx} have three resonant peaks at 7.3 GHz, 10.6 GHz and 14.4 GHz, respectively. Similarly, Fig. 3(b) shows the reflentance of y-polarized waves. Herein, we use $\mathrm{PCR} = |r_{xy}|^2/(|r_{xy}|^2+|r_{yy}|^2)$ to calculate the polarization conversion rate (PCR), and PCR is greater than 0.9 in 6.9–14.5 GHz with a relative bandwidth of 71% in Fig. 3(c), especially, the amplitude at the three resonant points is almost 1, which signifies a genertion of perfect polarization conversion.

Firstly, the u-polarized wave is decomposed into two components of equal amplitude along the x–y axis. The principle diagram of reflective MS is demonstrated in Fig. 4(a). The incident field can be expressed as $\boldsymbol{E}_i = E_u^i\boldsymbol{e}_u = E_y^i\boldsymbol{e}_y + E_x^i\boldsymbol{e}_x$, herein, $E_x^r = E_y^r$, which signifies no cross-polarized component generated along the u-polarized incidence [50]. $E_x^r = -E_y^r$ was also proved for v-polarized incidence. Therefore, we can then deduce that the reflection coefficient of co-polarization r_{uu} and r_{vv} are 1 without considering the substrate losses. The amplitude of r_{uu} and r_{vv} are displayed in Fig. 4(b). An x-polarized incident wave is described as $\boldsymbol{E}_i = E_u^i\boldsymbol{u} + E_v^i\boldsymbol{v}$,

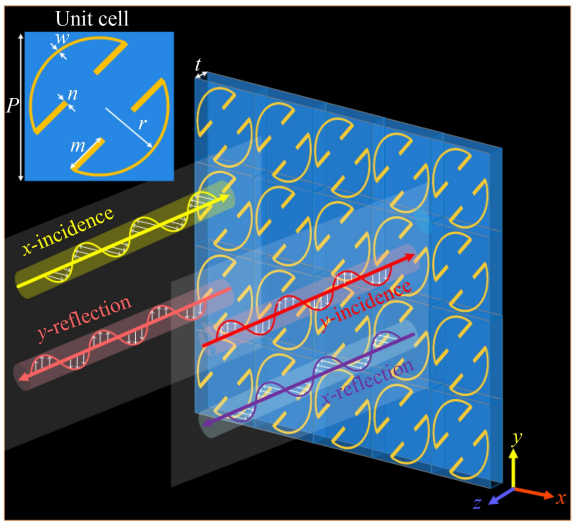

Fig. 2 The working mechanism diagram of metasurface.

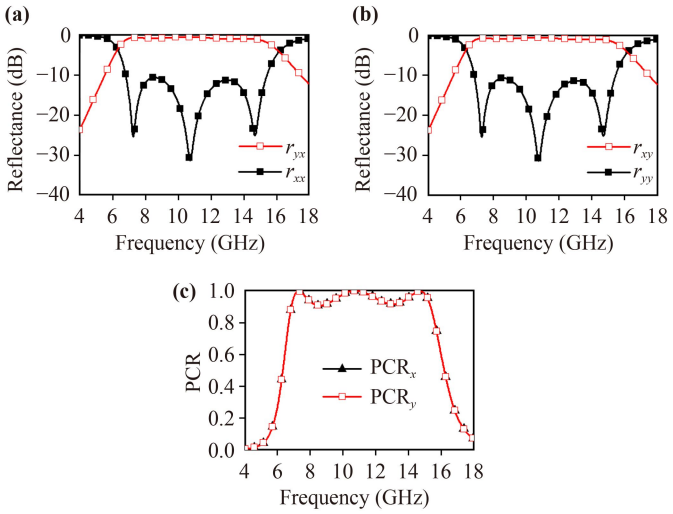

Fig. 3 Reflectance. **(a)** r_{xx} and r_{yx}. **(b)** r_{yy} and r_{xy}. **(c)** PCR.

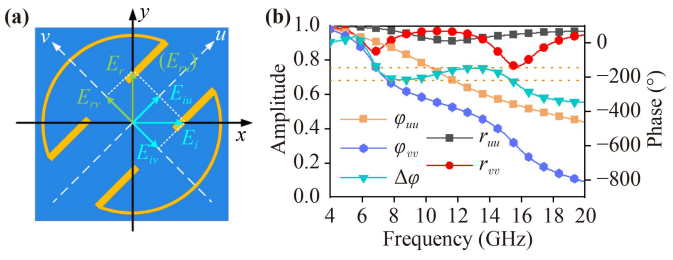

Fig. 4 **(a)** The schematic diagram of polarizer. **(b)** The reflectances of r_{uu}, r_{vv} and phase difference $\Delta\varphi$.

where $\boldsymbol{u}$ and $\boldsymbol{v}$ refer to the counterclockwise rotation of the x–y plane by 45°. Because of the asymmetric structure, if $r_{uu} \approx r_{vv} \approx 1$ and $\Delta\varphi = |\varphi_{uu} - \varphi_{vv}| = \pm 180°$, E_v^r is in the opposite direction of E_u^r, then the synthetic field E_v^r of E_v^r and E_u^r would be along the y-axis. In other words, the x-polarized incidence is rotated after reflection. As shown in Fig. 4(b), it is intuitive to show the r_{uu} and r_{vv} are roughly the same and the phase difference is $180° \pm 37°$ in 6.8–15.4 GHz, which directly leads to high-efficiency polarization conversion.

In what follows, for ease of comprehending the physical mechanism, the surface current distributions of the upper and bottom metallic films were illustrated in Fig. 5, which includes 7.3 GHz, 10.6 GHz and 14.3 GHz these three frequencies. Obviously the current direction of the upper metal film and the backplane are antiparallel at 7.3 GHz in Fig. 5(a), thus, the magnetic resonance is generated at this frequency point. The current direction of the upper film is still antiparallel to the current direction of the backplane in Figs. 5(b) and (c). A current loop is produced in the intermediate medium film, which is still noted as magnetic resonance. We can speculate that these three magnetic resonances are the key to realizing the efficient ultra-wideband polarization conversion.

4 Results and discussion

Table 1 portrays the eight coding meta-atoms by rotating different orientation angles of the top metal patterns. For 1-bit CMS, two coding modes ("0" and "1") with 90° relative rotation and 180° reflection phase difference are defined. Likewise, as for 2-bit CMS, four coding meta-atoms ("00", "01", "10" and "11") with the phase difference of 90° were required. With regard to 3-bit CMS, eight coding meta-atoms ("000", "001", "010", "011", "100", "101", "110" and "111") with a constant reflection phase difference of 45° were considered. Figures 6(a) and (b) show the relation between the rotation angle and the amplitude and phase under incidence of LCP/RCP waves, respectively. The amplitude apparently barely changes and the phase generates a difference of nearly 45° with a step of 22.5° rotation angle. There is a linear relation between the rotation angle and phase change of metallic dual-ring pattern. And full phase coverage has been implemented in this process.

As for 1-bit CMS arranged along x-direction in Fig. 7(a), the basic coding cell with the rotation of and to simulate 3D and 2D far field scattering patterns under normal incidence of the circularly polarized waves in 10.6 GHz. The incoming waves are reflected and decomposed into two symmetric waves with the angle of $\theta_1 = \arcsin(\lambda/\Gamma_1) = 43.9°$, $\varphi = 0°$ or $\varphi = 180°$, $\Gamma_1 = 2\times$ 20.4 mm is the period length of the CMS, which is shown in Fig. 7(b). Analogously, when the unit cells distributed in order of "00001111…" in Fig. 7(c) along y-direction, the circularly polarized wave is reflected along y-axis with the angle of $\theta_2 = \arcsin(\lambda/\Gamma_1) = 43.9°$, $\varphi = 90°$ or $\varphi = 270°$ in Fig. 7(d).

We arrange the 2-bit CMS to verify the different scattering field patterns generated by the coding particles in 10.6 GHz. The pre-designed coding layout and 3D far

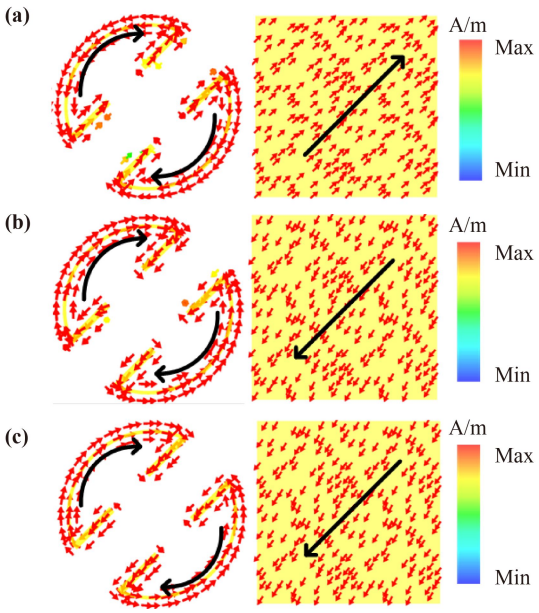

Fig. 5 Surface current distribution. **(a)** 7.3 GHz. **(b)** 10.6 GHz. **(c)** 14.3 GHz.

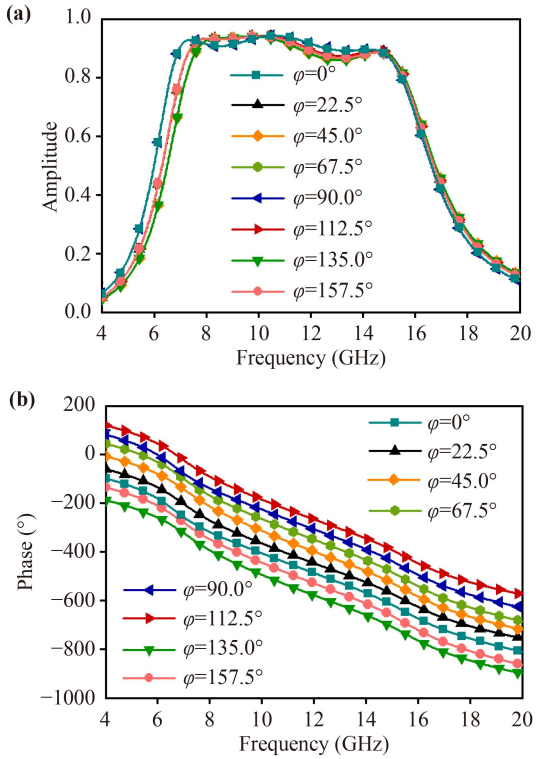

Fig. 6 **(a)** Amplitude and **(b)** phase with different rotation angles.

Table 1 The basic unit cells for CMS.

α	0°	22.5°	45°	67.5°	90°	112.5°	135°	157.5°
Unit								
1-bit	0	–	–	–	1	–	–	–
2-bit	00	–	01	–	10	–	11	–
3-bit	000	001	010	011	100	101	110	111

field is shown in Fig. 8(a) and the corresponding 2D far field diagram is drawn in Fig. 8(b). We can see clearly that circularly polarized wave is symmetrically decomposed into four reflected waves with the angle of $\theta_2 = \arcsin(\lambda/\Gamma_2) = 43.9°$, $\varphi = 0°$, $\varphi = 90°$ or $\varphi = 180°$, $\varphi = 270°$, $\Gamma_3 = 2 \times 20.4$ mm.

A 3-bit CMS aligned along the x-axis has been displayed in Fig. 9 to observe its far field scattering. The LCP wave along the forward direction is reflected into a particular direction with the angle of $\theta_4 = \arcsin(\lambda/\Gamma_3) = 8.1°$, $\varphi = 0°$, $\Gamma_3 = 8 \times 20.4$ mm, shown in Figs. 9(a) and (b). In addition, for the RCP wave with forward propagation depicted in Figs. 9(c) and (d), the reflection angle of the LCP wave is $\theta_5 = \arcsin(\lambda/\Gamma_3) = 8.1°$, $\varphi = 0°$. All the beam control phenomena above meet the simulation and theoretical calculation values.

Based on the beam control, full-wave simulation is adopted when the linearly polarized waves are normal

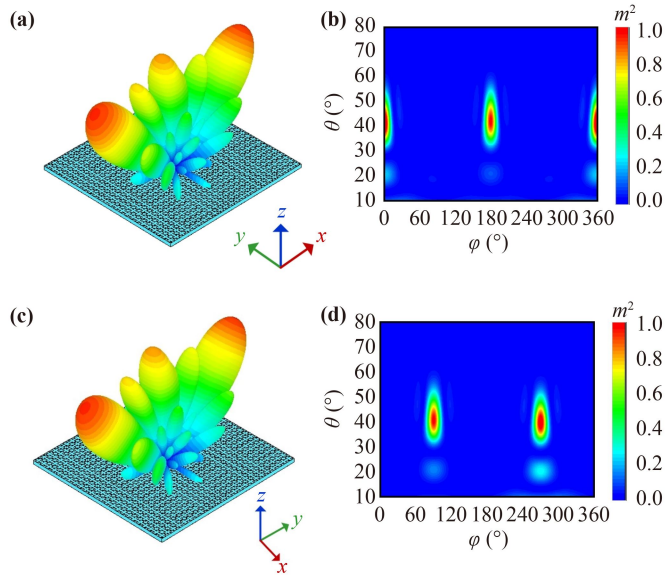

Fig. 7 3D and 2D far field scattering patterns of 1-bit CMS. **(a)** 3D far field, **(b)** 2D far field along x-direction. **(c)** 3D far field, **(d)** 2D far field along y-direction.

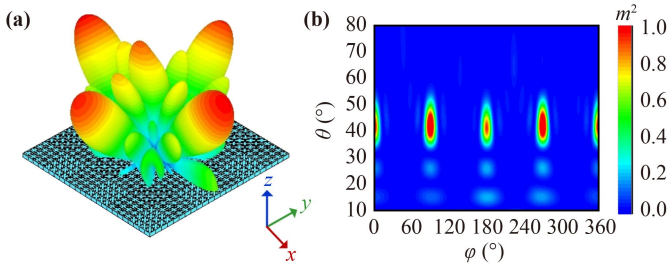

Fig. 8 3D and 2D far field scattering patterns of 2-bit CMS. **(a)** 3D far field, **(b)** 2D far field.

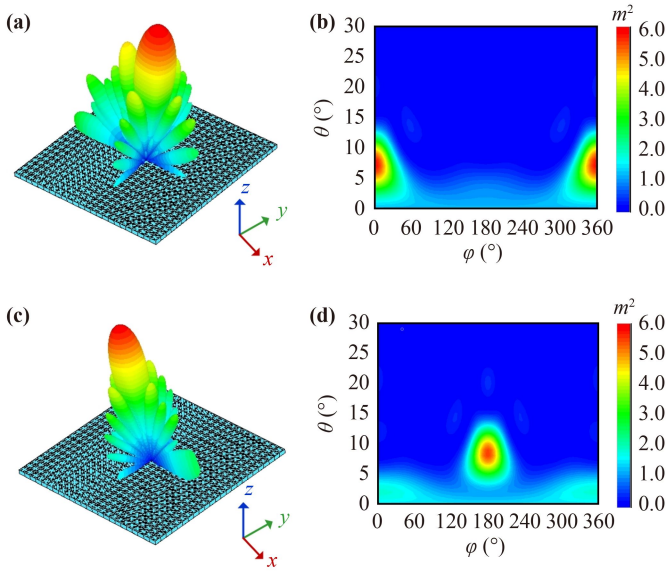

Fig. 9 3D and 2D far field scattering patterns of 3-bit CMS. **(a)** 3D far field, **(b)** 2D far field of LCR incidence. **(c)** 3D far field, **(d)** 2D far field of RCP incidence.

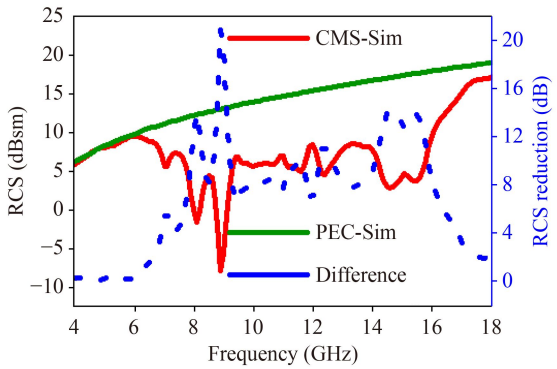

Fig. 10 The RCS of the metal plane and CMS.

Table 2 Performance comparison with presented works.

Polarization converter			
Ref.	OB[1](GHz)	PCR(%)	RB[2](%)
[52]	10.3–20.5	90%	66.2
[53]	6.53–12.07	88%	59.6
[54]	9.38–13.36 & 14.84–20.36	90%	35
[55]	8–12	90%	40
This work	6.9–14.5	90%	71
RCS reduction			
Ref.	Working mechanism	OB[1](GHz)	RB[2](%)
[56]	Anomalous reflection	8.9–11.4	24.6
[57]	Anomalous reflection	9.85–19.37	65
[58]	Anomalous reflection	7–16	78
[59]	Destructive interference	9.5–13.9 & 15.2–20.4	32 & 30
[60]	Absorber	2.12–4.15 & 6.08–9.58	64 & 45
[61]	Diffused scattering	5.4–7.4	31.25
[62]	Diffused scattering	13.2–23.2	54.9
[63]	Polarization conversion	8–16	67.8
This work	Polarization conversion & diffused scattering	6.9–14.5	71

[1] OB: Operation bandwidth;
[2] RB: Relative bandwidth.

incident to study the diffusion-like phenomenon of the CMS, Fig. 10 depicts the simulated monostatic RCS of CMS as well as the same metal surface under the propagation of linearly polarized wave for the sake of comparison. As can be seen, the reduction of RCS is more than 10 dB at 6–16 GHz for the CMS. The difference of RCS reduction (blue line) between the metal plate and CMS is greater than 10 dB, and maximum RCS reduction exceeds 20 dB at 9 GHz. The experimental and simulated monostatic RCS values are basically consistent, even though the sample manufacturing process deviation and experimental environment influence, which clearly proves the practicability of the CMS for RCS reduction.

Finally, we extracted the relevant results from other literatures for comparison. As can be seen from Table 2, our design has an excellent performance within the ultra-wide bandwith.

5 Experimental verification

For the experiment, an experimental sample with 40 × 40 unit-cells and a size of 20.4 cm × 20.4 cm is processed and tested to validate the polarization conversion in a microwave anechoic chamber, which is displayed in Fig. 11(a). And the experimental test environment is depicted in Fig. 11(b). Two horn antennas are connected to the network vector analyzer (R&S ZNB/40), one of which is used to emit gain linear polarization, and the other for receiving linear polarization. Then the reflection coefficients can be obtained by rotating the horn antenna perpendicular or parallel to the ground. The microwave anechoic chamber is surrounded by absorbent materials to eliminate electromagnetic interference. Figures 12(a)–(c) depict the conversion of incident waves, including the simulation and experimental results. They fit perfectly, expect for a slight frequency shift.

The CMS with a size of 20.4 cm × 20.4 cm in Fig. 11(c) is applied to verify RCS reduction. The reflection coefficient S_{11} of sample is firstly considered to measure, as shown in Fig. 12(d). Then the equation is calculated to acquire the value of RCS, as follows [51]:

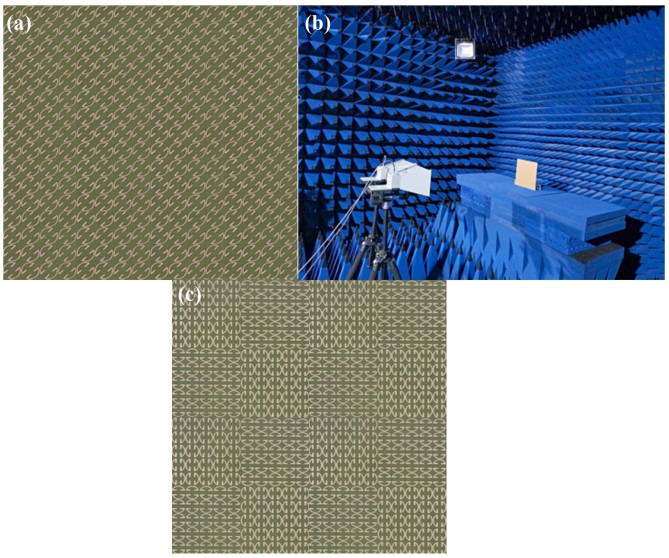

Fig. 11 **(a)** Sample diagram for testing polarization conversion. **(b)** Experimental test environment. **(c)** Sample diagram for RCS reduction.

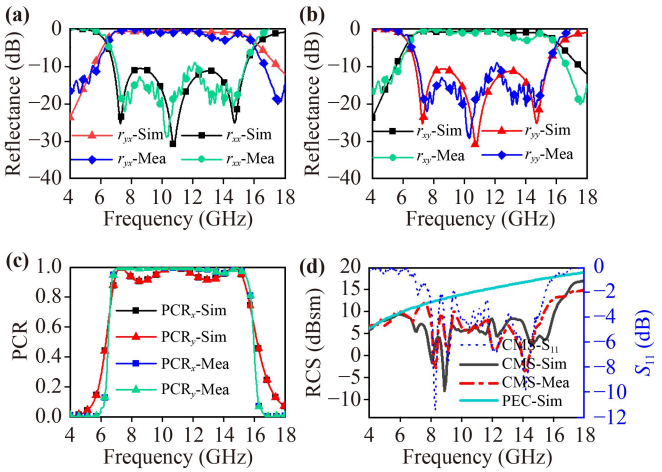

Fig. 12 Measurement results of **(a)** x-polarized incident wave, **(b)** y-polarized incident wave, **(c)** PCR, **(d)** S_{11} and RCS reduction.

$$\sigma = 4\pi R^2 |\frac{E_s}{E_i}|^2. \tag{7}$$

E_i and E_s denote the incident electric field intensity and scattered electric field intensity, respectively. In addition to the RCS of the target, which can be expressed as square meters, it can also be described as ten times the value of the RCS logarithm [51]

$$RCS\ (\text{dBsm}) = 10 \times \log_{10}(RCS/(1\ \text{m}^2)). \tag{8}$$

Figure 12(d) shows the simulated and measured RCS values for the CMS. These two results are in good agreement and both lower than it compared with RCS values of PEC.

The subtle differences are attributed to the fabrication tolerance and experimental environment. We set the periodic boundary conditions during simulation, which means the proposed polarizer is a plane of infinite size, but the actual sample measured is finite, which causes the edge scattering.

6 Conclusion

In conclusion, a new reflection polarization converter was proposed and measured for applying on the beam control and RCS reduction. The basic unit was enabled the linear polarization wave to cross-polarized state with relative bandwidth of 71%, PCR of almost 90% from 6.9 GHz to 14.5 GHz according to simulation. CMSs based on the PB phase principle were designed to react on circular polarization beam control and satisfy the generalized Snell's law. Finally, we adopted the 2-bit coding metasurface to verify the RCS reduction properties. This indicates that the availability of manipulating the polarized wave plays an important role in electromagnetic stealth and antenna designs.

Acknowledgements This work was supported by the National Natural Science Foundation of China (No. 42274189) and the Project of Science and Technology of Shaanxi (No. 2021JM-395).

References

1. B. Fang, D. Feng, P. Chen, L. Shi, J. Cai, J. Li, C. Li, Z. Hong, and X. Jing, Broadband cross-circular polarization carpet cloaking based on a phase change material metasurface in the mid-infrared region, *Front. Phys.* 17(5), 53502 (2022)
2. J. Ding, S. An, B. Zheng, and H. Zhang, Multiwavelength metasurfaces based on single-layer dual-wavelength metaatoms: Toward complete phase and amplitude modulations at two wavelengths, *Adv. Opt. Mater.* 5(10), 1700079 (2017)
3. L. Bao, R. Y. Wu, X. Fu, and T. J. Cui, Mathematical operations of transmissive near fields controlled by metasurface with phase and amplitude modulations, *Ann. Phys.* 532(6), 2000069 (2020)
4. A. C. Overvig, S. Shrestha, S. C. Malek, M. Lu, A. Stein, C. Zheng, and N. Yu, Dielectric metasurfaces for complete and independent control of the optical amplitude and phase, *Light Sci. Appl.* 8(1), 92 (2019)
5. T. Wu, X. Zhang, Q. Xu, E. Plum, K. Chen, Y. Xu, Y. Lu, H. Zhang, Z. Zhang, X. Chen, G. Ren, L. Niu, Z. Tian, J. Han, and W. Zhang, Dielectric metasurfaces for complete control of phase, amplitude, and polarization, *Adv. Opt. Mater.* 10(1), 2101223 (2022)
6. Z. Y. Song, Q. Q. Chu, X. P. Shen, and Q. H. Liu, Wideband high-efficient linear polarization rotators, *Front. Phys.* 13(5), 137803 (2018)
7. X. Huang, X. Ma, X. Li, J. Fan, L. Guo, and H. Yang, Simultaneous realization of polarization conversion for reflected and transmitted waves with bi-functional metasurface, *Sci. Rep.* 12(1), 2368 (2022)
8. F. Zeng, L. Ye, L. Li, Z. Wang, W. Zhao, and Y. Zhang, Tunable mid-infrared dual-band and broadband crosspolarization converters based on U-shaped graphene metamaterials, *Opt. Express* 27(23), 33826 (2019)
9. Y. Wang, F. Qi, Z. Liu, P. Liu, and W. Li, Ultrathin and flexible reflective polarization converter based on metasurfaces with overlapped arrays, *IEEE Antennas Wirel. Propag. Lett.* 19(12), 2512 (2020)
10. J. Loncar, A. Grbic, and S. Hrabar, A reflective polarization converting metasurface at X-band frequencies, *IEEE Trans. Antenn. Propag.* 66(7), 3213 (2018)
11. Q. Zheng, C. Guo, and J. Ding, Wideband metasurface-based reflective polarization converter for linear-to-linear and linear-to-circular polarization conversion, *IEEE Antennas Wirel. Propag. Lett.* 17(8), 1459 (2018)
12. X. Huang, H. Yang, D. Zhang, and Y. Luo, Ultrathin dualband metasurface polarization converter, *IEEE Trans. Antenn. Propag.* 67(7), 4636 (2019)
13. X. Huang, H. Gao, J. He, X. Li, X. Li, J. Fan, and L. Guo, Broadband linear polarizer with high-efficient asymmetric transmission using a chiral metasurface, *AEU Int. J. Electron. Commun.* 152, 154244 (2022)
14. N. Yu, P. Genevet, M. A. Kats, F. Aieta, J. P. Tetienne,

F. Capasso, and Z. Gaburro, Light propagation with phase discontinuities: Generalized laws of reflection and refraction, *Science* 334(6054), 333 (2011)
15. F. Yue, D. Wen, J. Xin, B. D. Gerardot, J. Li, and X. Chen, Vector vortex beam generation with a single plasmonic metasurface, *ACS Photon.* 3(9), 1558 (2016)
16. M. Feng, X. Tian, J. Wang, M. Yin, S. Qu, and D. Li, Broadband abnormal reflection based on a metal-backed gradient index liquid slab: An alternative to metasurfaces, *J. Phys. D Appl. Phys.* 48(24), 245501 (2015)
17. Z. Xu, Z. Li, Y. Tian, Y. Wei, and F. Wu, Highly efficient bifunctional dielectric metasurfaces at visible wavelength: Beam focusing and anomalous refraction in highorder modes, *Front. Phys.* 8, 575824 (2020)
18. Y. U. Lee, I. Ozerov, F. Bedu, J. S. Kim, F. Fages, and J. W. Wu, Optical spin-dependent beam separation in cyclic group symmetric metasurface, *Nanophotonics* 9(10), 3459 (2020)
19. X. Wu, H. Cao, Z. Meng, and Z. Sun, Ultra-broadband Pancharatnam–Berry phase metasurface for arbitrary rotation of linear polarization and beam splitter, *Opt. Express* 30(9), 15158 (2022)
20. A. Leitis, A. Heßler, S. Wahl, M. Wuttig, T. Taubner, A. Tittl, and H. Altug, All-dielectric programmable Huygens' metasurfaces, *Adv. Funct. Mater.* 30(19), 1910259 (2020)
21. Z. Wang, S. Dong, W. Luo, M. Jia, Z. Liang, Q. He, S. Sun, and L. Zhou, High-efficiency generation of Bessel beams with transmissive metasurfaces, *Appl. Phys. Lett.* 112(19), 191901 (2018)
22. Y. Liu, C. Liu, K. Song, M. Li, and X. Zhao, A broadband high-transmission gradient phase discontinuity metasurface, *J. Phys. D Appl. Phys.* 51(9), 095103 (2018)
23. L. W. Wu, H. F. Ma, Y. Gou, R. Y. Wu, Z. X. Wang, M. Wang, X. Gao, and T. J. Cui, High-transmission ultrathin Huygens' metasurface with 360° phase control by using double-layer transmitarray elements, *Phys. Rev. Appl.* 12(2), 024012 (2019)
24. Q. Zhou, M. Liu, W. Zhu, L. Chen, Y. Ren, H. J. Lezec, Y. Lu, A. Agrawal, and T. Xu, Generation of perfect vortex beams by dielectric geometric metasurface for visible light, *Laser Photon. Rev.* 15(12), 2100390 (2021)
25. F. Yu, Z. Zhao, J. Chen, J. Wang, R. Jin, J. Chen, J. Wang, G. Li, X. Chen, and W. Lu, Orthogonal manipulations of phase and phase dispersion in realization of azimuthal angle-resolved focusings, *Opt. Express* 29(26), 43757 (2021)
26. S. Pancharatnam, Generalized theory of interference, and its applications, *Resonance* 18(4), 387 (2013)
27. A. Moreno-Peñarrubia, J. Teniente, S. Kuznetsov, B. Orazbayev, and M. Beruete, Ultrathin and high-efficiency Pancharatnam–Berry phase metalens for millimeter waves, *Appl. Phys. Lett.* 118(22), 221105 (2021)
28. R. Lin and X. Li, Multifocal metalens based on multilayer Pancharatnam–Berry phase elements architecture, *Opt. Lett.* 44(11), 2819 (2019)
29. S. Choudhury, U. Guler, A. Shaltout, V. M. Shalaev, A. V. Kildishev, and A. Boltasseva, Pancharatnam–Berry phase manipulating metasurface for visible color hologram based on low loss silver thin film, *Adv. Opt. Mater.* 5(10), 1700196 (2017)
30. X. Song, L. Huang, L. Sun, X. Zhang, R. Zhao, X. Li, J. Wang, B. Bai, and Y. Wang, Near-field plasmonic beam engineering with complex amplitude modulation based on metasurface, *Appl. Phys. Lett.* 112(7), 073104 (2018)
31. S. J. Li, Z. Y. Li, G. S. Huang, X. B. Liu, R. Q. Li, and X. Y. Cao, Digital coding transmissive metasurface for multi-OAM-beam, *Front. Phys.* 17(6), 62501 (2022)
32. H. X. Xu, G. Hu, Y. Wang, C. Wang, M. Wang, S. Wang, Y. Huang, P. Genevet, W. Huang, and C. W. Qiu, Polarization-insensitive 3D conformal-skin metasurface cloak, *Light Sci. Appl.* 10(1), 75 (2021)
33. H. Xu, Y. Wang, C. Wang, M. Wang, S. Wang, F. Ding, Y. Huang, X. Zhang, H. Liu, X. Ling, and W. Huang, Deterministic approach to achieve full-polarization cloak, *Research* 2021, 1 (2021)
34. S. M. Kamali, E. Arbabi, A. Arbabi, and A. Faraon, A review of dielectric optical metasurfaces for wavefront control, *Nanophotonics* 7(6), 1041 (2018)
35. L. Liang, M. Qi, J. Yang, X. Shen, J. Zhai, W. Xu, B. Jin, W. Liu, Y. Feng, C. Zhang, H. Lu, H. T. Chen, L. Kang, W. Xu, J. Chen, T. J. Cui, P. Wu, and S. Liu, Anomalous terahertz reflection and scattering by flexible and conformal coding metamaterials, *Adv. Opt. Mater.* 3(10), 1374 (2015)
36. Y. Tian, X. Jing, H. Yu, H. Gan, C. Li, and Z. Hong, Manipulation of the arbitrary scattering angle based on all-dielectric transmissive Pancharatnam–Berry phase coding metasurfaces in the visible range, *Opt. Express* 28(21), 32107 (2020)
37. J. Yang, Y. Chen, M. Jian, J. Dou, and M. Fang, Capacity improvement in reconfigurable intelligent surface assisted MIMO communications, *IEEE Access* 9, 137460 (2021)
38. X. Pei, H. Yin, L. Tan, L. Cao, Z. Li, K. Wang, K. Zhang, and E. Bjornson, RIS-aided wireless communications: Prototyping, adaptive beamforming, and indoor/outdoor field trials, *IEEE Trans. Commun.* 69(12), 8627 (2021)
39. J. Han, X. Cao, J. Gao, S. Li, H. Yang, C. Zhang, and T. Li, Broadband dual-circular polarized coding metasurfaces and their powerful manipulation of differently circular polarizations, *Opt. Express* 27(23), 34141 (2019)
40. S. Li, S. Dong, S. Yi, W. Pan, Y. Chen, F. Guan, H. Guo, Z. Wang, Q. He, L. Zhou, and S. Sun, Broadband and high-efficiency spin-polarized wave engineering with PB metasurfaces, *Opt. Express* 28(10), 15601 (2020)
41. Y. Gou, H. F. Ma, L. W. Wu, Z. X. Wang, P. Xu, and T. J. Cui, Broadband spin-selective wavefront manipulations based on Pancharatnam–Berry coding metasurfaces, *ACS Omega* 6(44), 30019 (2021)
42. C. Fu, L. Han, C. Liu, X. Lu, and Z. Sun, Combining Pancharatnam–Berry phase and conformal coding metasurface for dual-band RCS reduction, *IEEE Trans. Antenn. Propag.* 70(3), 2352 (2022)
43. G. Yu, Y. Qiu, Y. Li, X. Wang, and N. Wang, Underwater acoustic stealth by a broadband 2-bit coding metasurface, *Phys. Rev. Appl.* 15(6), 064064 (2021)
44. H. X. Xu, L. Zhang, Y. Kim, G. M. Wang, X. K. Zhang, Y. Sun, X. Ling, H. Liu, Z. Chen, and C. W. Qiu, Wavenumber-splitting metasurfaces achieve multichannel diffusive invisibility, *Adv. Opt. Mater.* 6(10), 1800010

(2018)
45. X. Li, M. Feng, J. Wang, Y. Meng, J. Yang, T. Liu, R. Zhu, and S. Qu, Suppressing edge back-scattering of electromagnetic waves using coding metasurface purfle, *Front. Phys. (Lausanne)* 8, 578295 (2020)
46. A. Murugesan, K. T. Selvan, A. Iyer, K. V. Srivastava, and A. Alphones, A review of metasurface-assisted RCS reduction techniques, *Prog. Electromagn. Res. B Pier B* 94, 75 (2021)
47. H. X. Xu, S. Ma, X. Ling, X. K. Zhang, S. Tang, T. Cai, S. Sun, Q. He, and L. Zhou, Deterministic approach to achieve broadband polarization-independent diffusive scatterings based on metasurfaces, *ACS Photon.* 5(5), 1691 (2018)
48. G. Bao and J. Lai, Optimal shape design of a cavity for radar cross section reduction, *SIAM J. Contr. Optim.* 52(4), 2122 (2014)
49. Y. T. Zhao, B. Chen, and B. Wu, Miniaturized periodicity broadband absorber with via-based hybrid metal-graphene structure for large-angle RCS reduction, *IEEE Trans. Antenn. Propag.* 70(4), 2832 (2022)
50. B. Q. Lin, J. X. Guo, P. Chu, W. J. Huo, Z. Xing, B. G. Huang, and L. Wu, Multiple-band linear-polarization conversion and circular polarization in reflection mode using a symmetric anisotropic metasurface, *Phys. Rev. Appl.* 9(2), 024038 (2018)
51. A. Y. Modi, C. A. Balanis, C. R. Birtcher, and H. N. Shaman, Novel design of ultrabroadband radar cross section reduction surfaces using artificial magnetic conductors, *IEEE Trans. Antenn. Propag.* 65(10), 5406 (2017)
52. J. Zhang, L. Yang, L. Li, T. Zhang, H. Li, Q. Wang, Y. Hao, M. Lei, and K. Bi, High-efficiency polarization conversion phase gradient metasurface for wideband anomalous reflection, *J. Appl. Phys.* 122(1), 014501 (2017)
53. Q. Zheng, C. Guo, and J. Ding, Wideband metasurface-based reflective polarization converter for linear-to-linear and linear-to-circular polarization conversion, *IEEE Antennas Wirel. Propag. Lett.* 17(8), 1459 (2018)
54. P. Science, E. Engineering, I. Technology, A. Electromagnetics, and I. Science, Ultra-broadband wide-angle linear polarization converter based on H-shaped metasurface, *Opt. Express* 26(16), 20913 (2018)
55. T. K. T. Nguyen, T. M. Nguyen, H. Q. Nguyen, T. N. Cao, D. T. Le, X. K. Bui, S. T. Bui, C. L. Truong, D. L. Vu, and T. Q. H. Nguyen, Simple design of efficient broadband multifunctional polarization converter for Xband applications, *Sci. Rep.* 11(1), 2032 (2021)
56. Y. Cheng, C. Wu, C. Ge, J. Yang, X. Pei, F. Jia, and R. Gong, An ultra-thin dual-band phase-gradient metasurface using hybrid resonant structures for backward RCS reduction, *Appl. Phys. B* 123(5), 143 (2017)
57. Q. Zheng, Y. Li, J. Zhang, H. Ma, J. Wang, Y. Pang, Y. Han, S. Sui, Y. Shen, H. Chen, and S. Qu, Wideband, wide-angle coding phase gradient metasurfaces based on Pancharatnam–Berry phase, *Sci. Rep.* 7(1), 43543 (2017)
58. W. Zhang, Y. Liu, S. Gong, J. Wang, and Y. Jiang, Wideband RCS reduction of a slot array antenna using phase gradient metasurface, *IEEE Antennas Wirel. Propag. Lett.* 17(12), 2193 (2018)
59. C. Fu, L. Han, C. Liu, Z. Sun, and X. Lu, Dual-band polarization conversion metasurface for RCS reduction, *IEEE Trans. Antenn. Propag.* 69(5), 3044 (2021)
60. A. Sharma, S. Ghosh, and K. V. Srivastava, A polarization-insensitive band-notched absorber for radar cross section reduction, *IEEE Antennas Wirel. Propag. Lett.* 20(2), 259 (2021)
61. X. Liu, J. Gao, L. Xu, X. Cao, Y. Zhao, and S. Li, A coding diffuse metasurface for RCS reduction, *IEEE Antennas Wirel. Propag. Lett.* 16, 724 (2017)
62. F. Yuan, G. M. Wang, H. X. Xu, T. Cai, X. J. Zou, and Z. H. Pang, Broadband RCS reduction based on spiral-coded metasurface, *IEEE Antennas Wirel. Propag. Lett.* 16, 3188 (2017)
63. S. H. Kim and Y. J. Yoon, Wideband radar cross-section reduction on checkerboard metasurfaces with surface wave suppression, *IEEE Antennas Wirel. Propag. Lett.* 18(5), 896 (2019)